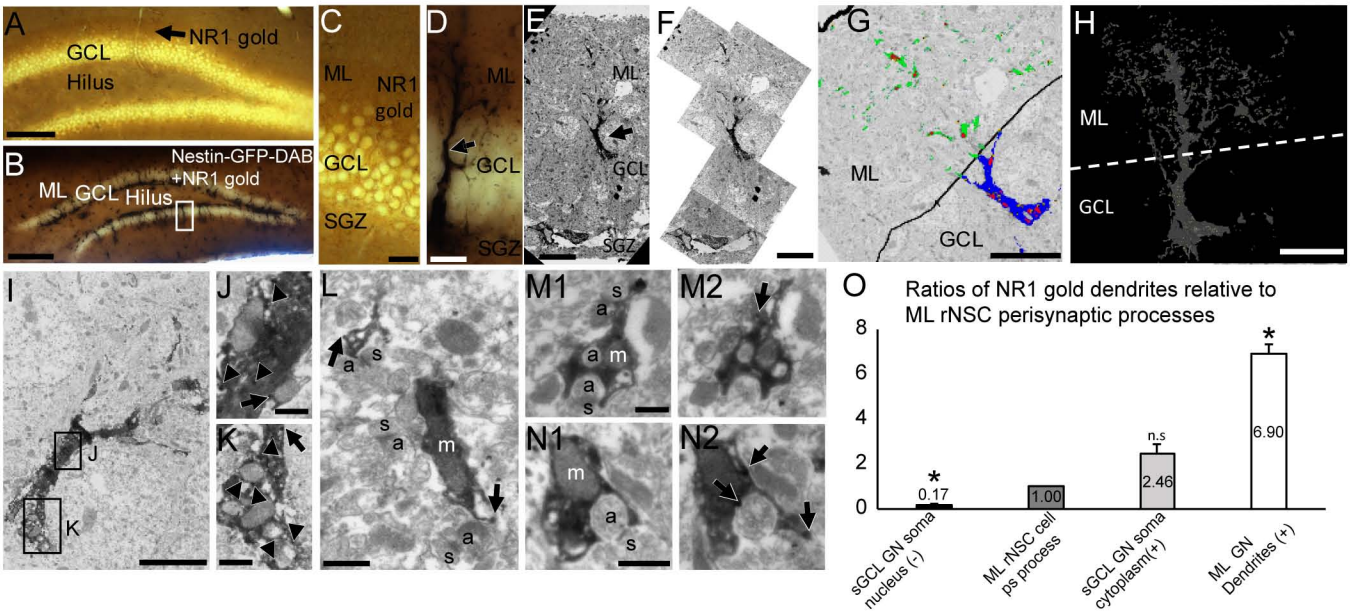


Figure S1. Yeh et al. 2018

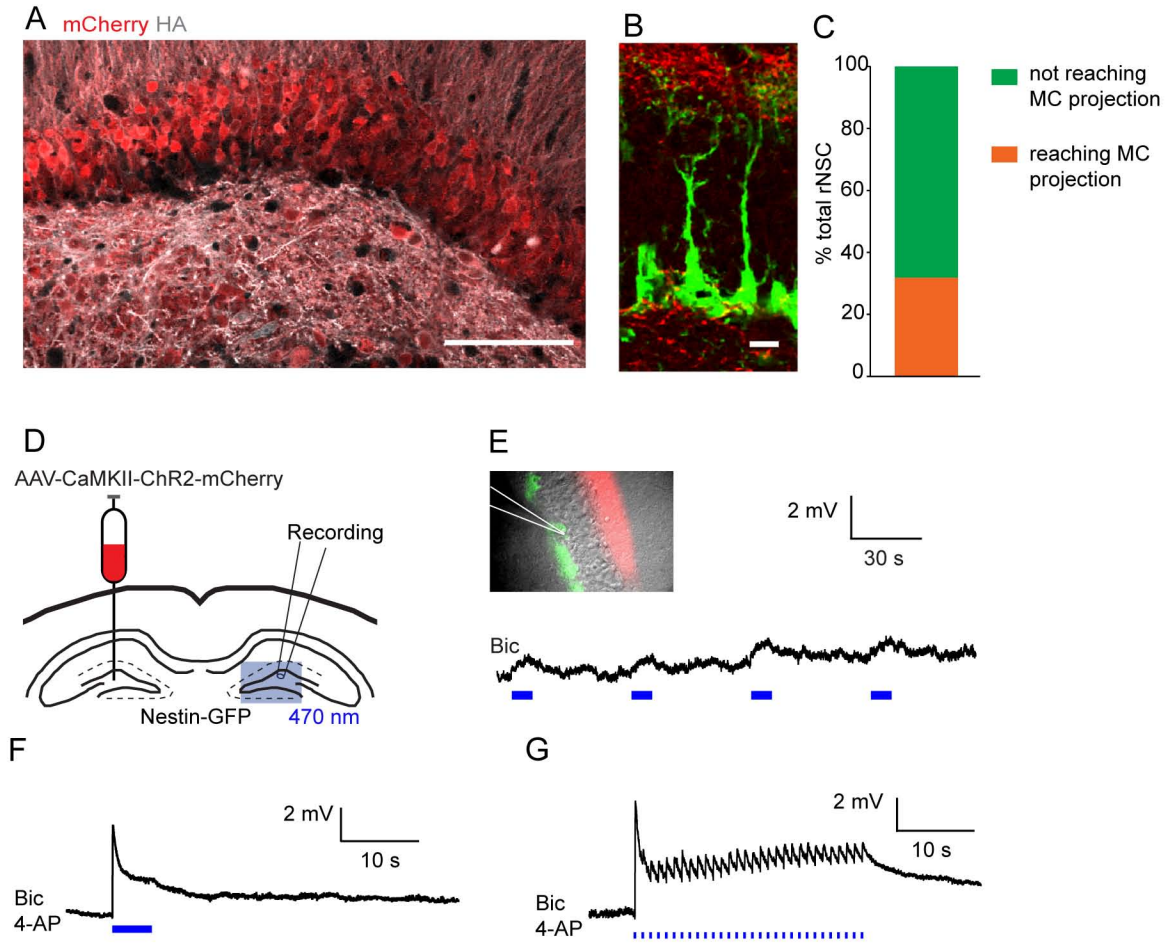


Figure S2. Yeh et al. 2018

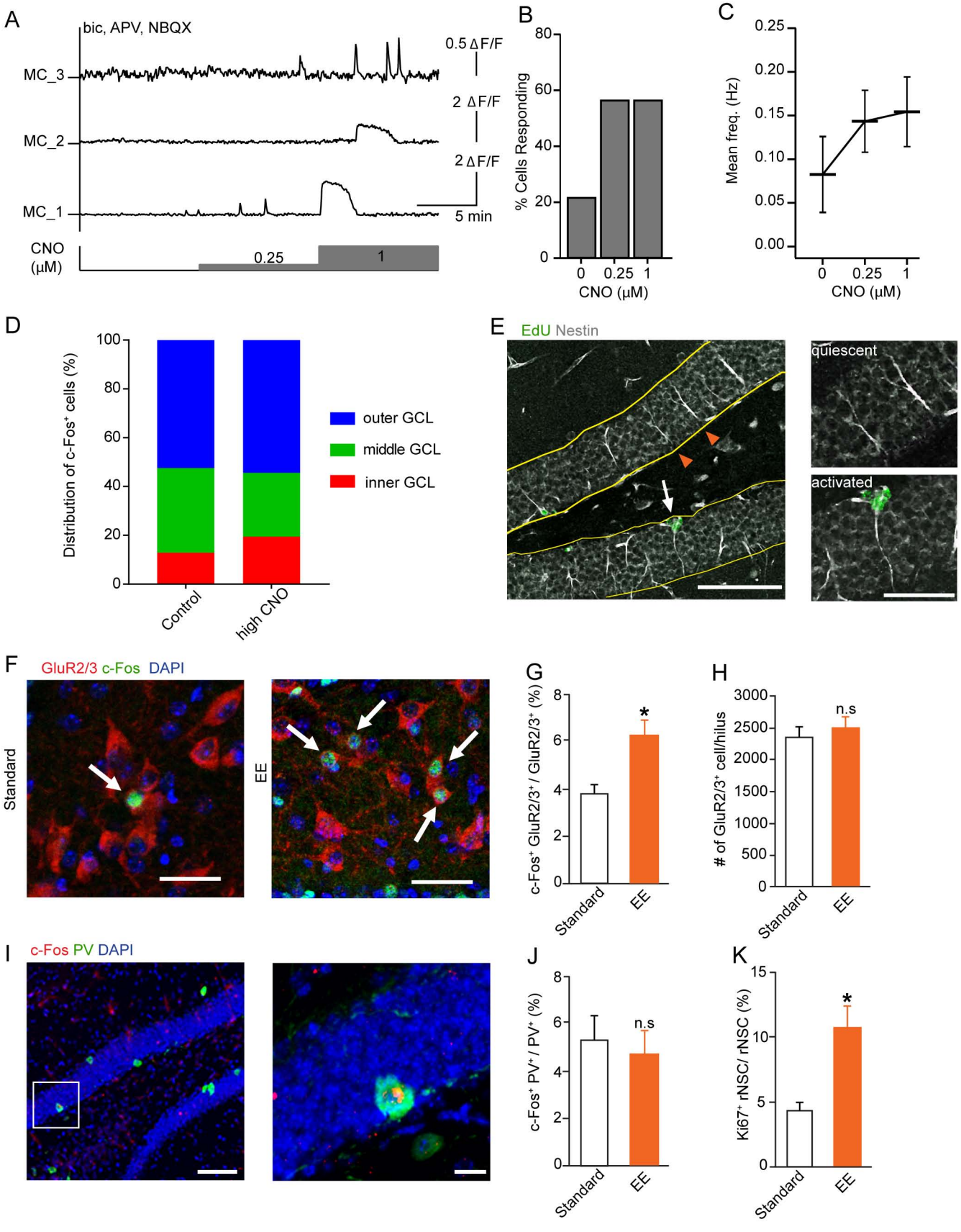


Figure S3. Yeh et al. 2018

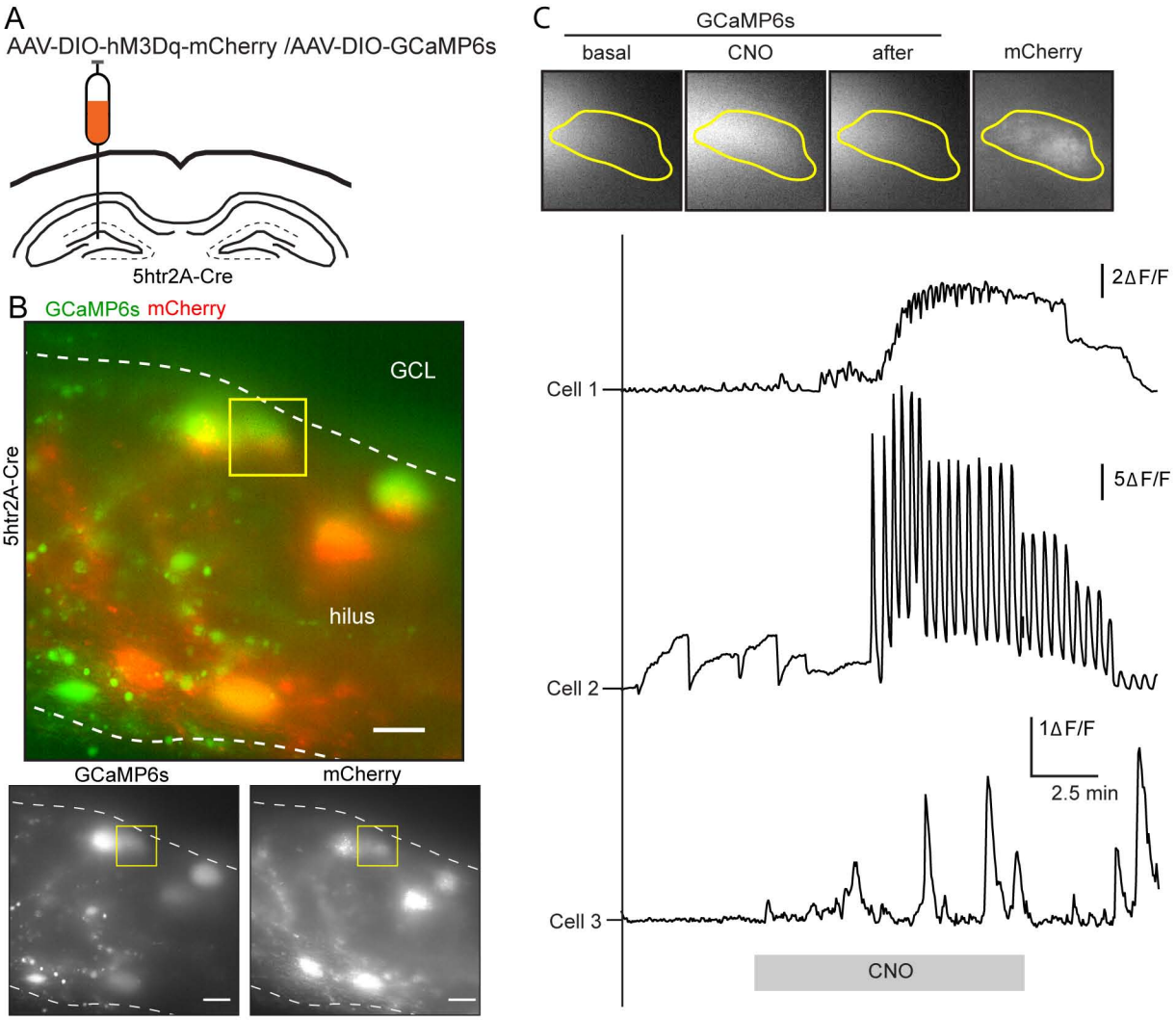


Figure S4. Yeh et al. 2018

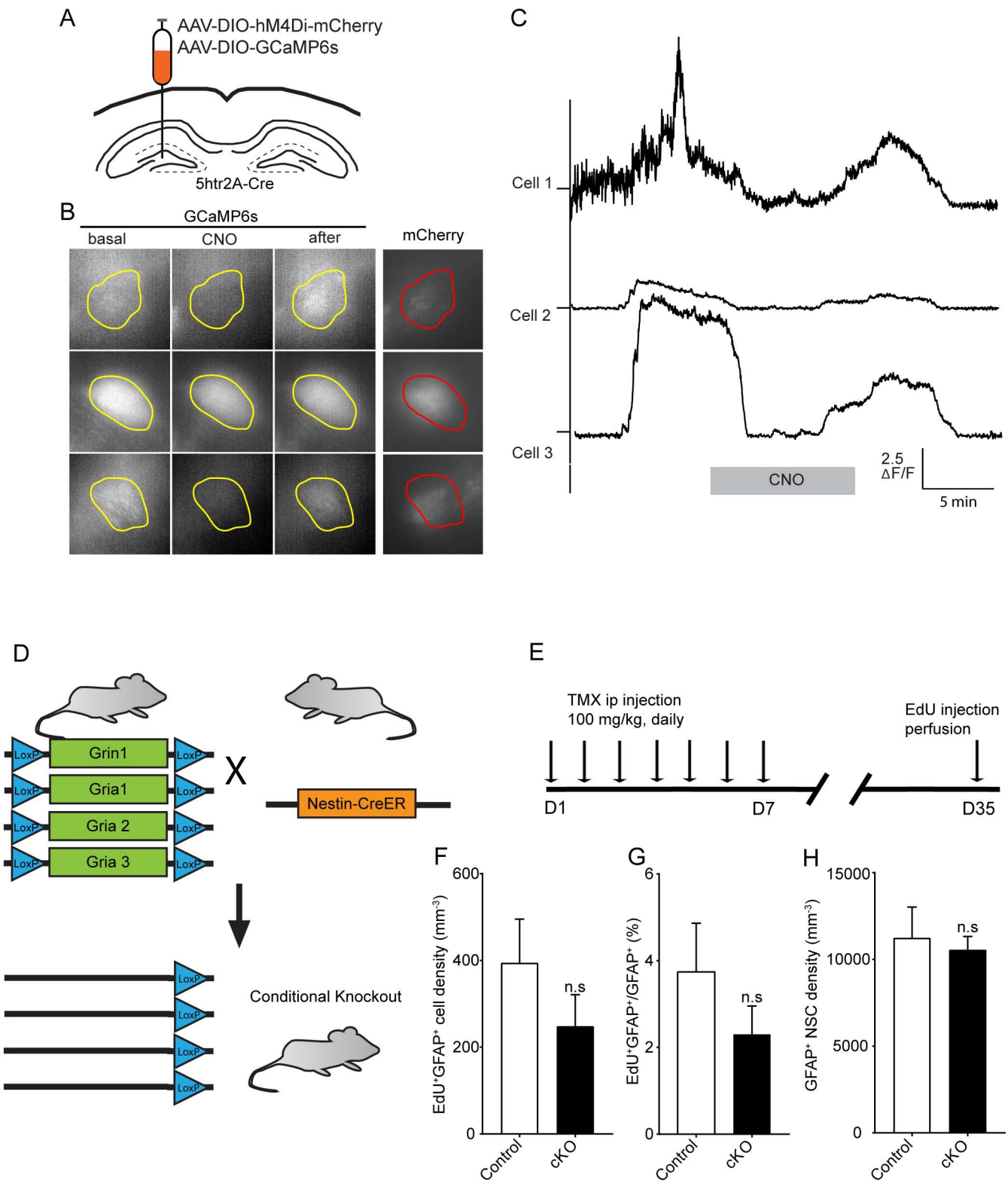


Figure S5. Yeh et al. 2018

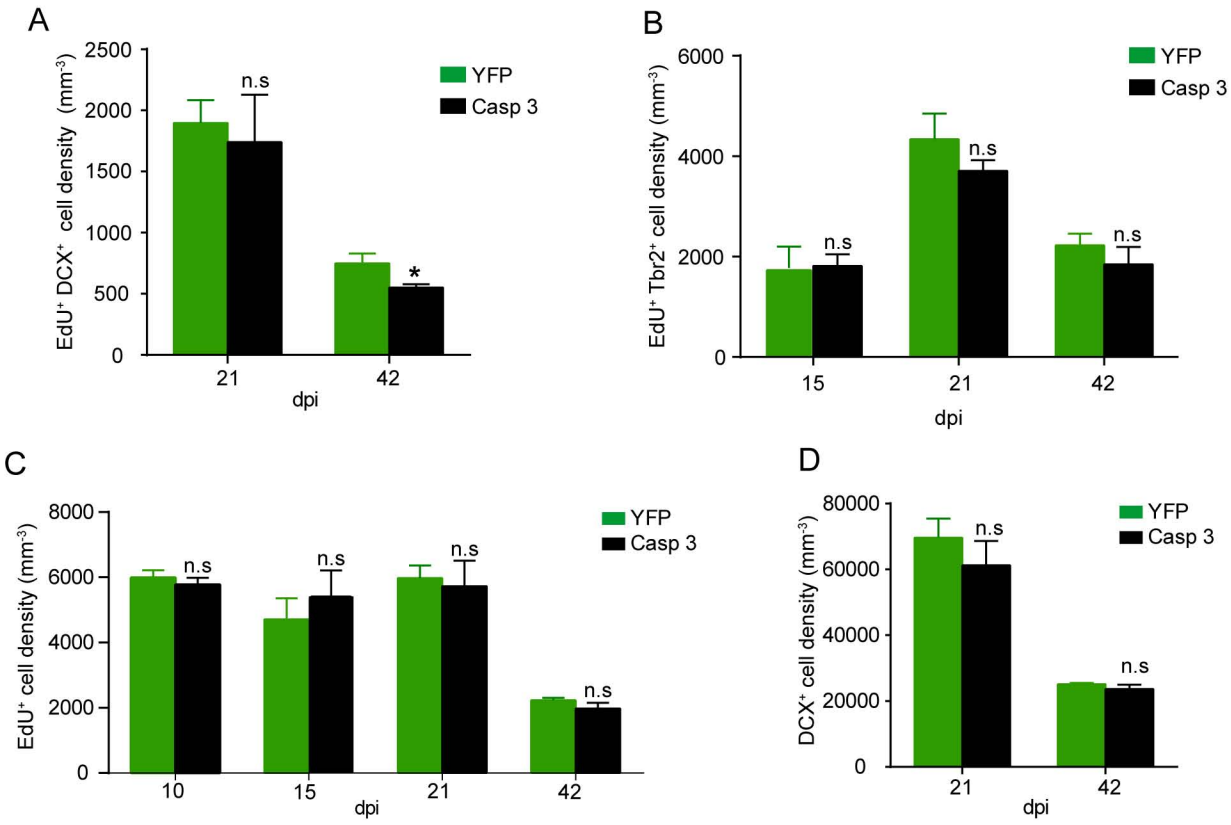


Figure S6. Yeh et al. 2018

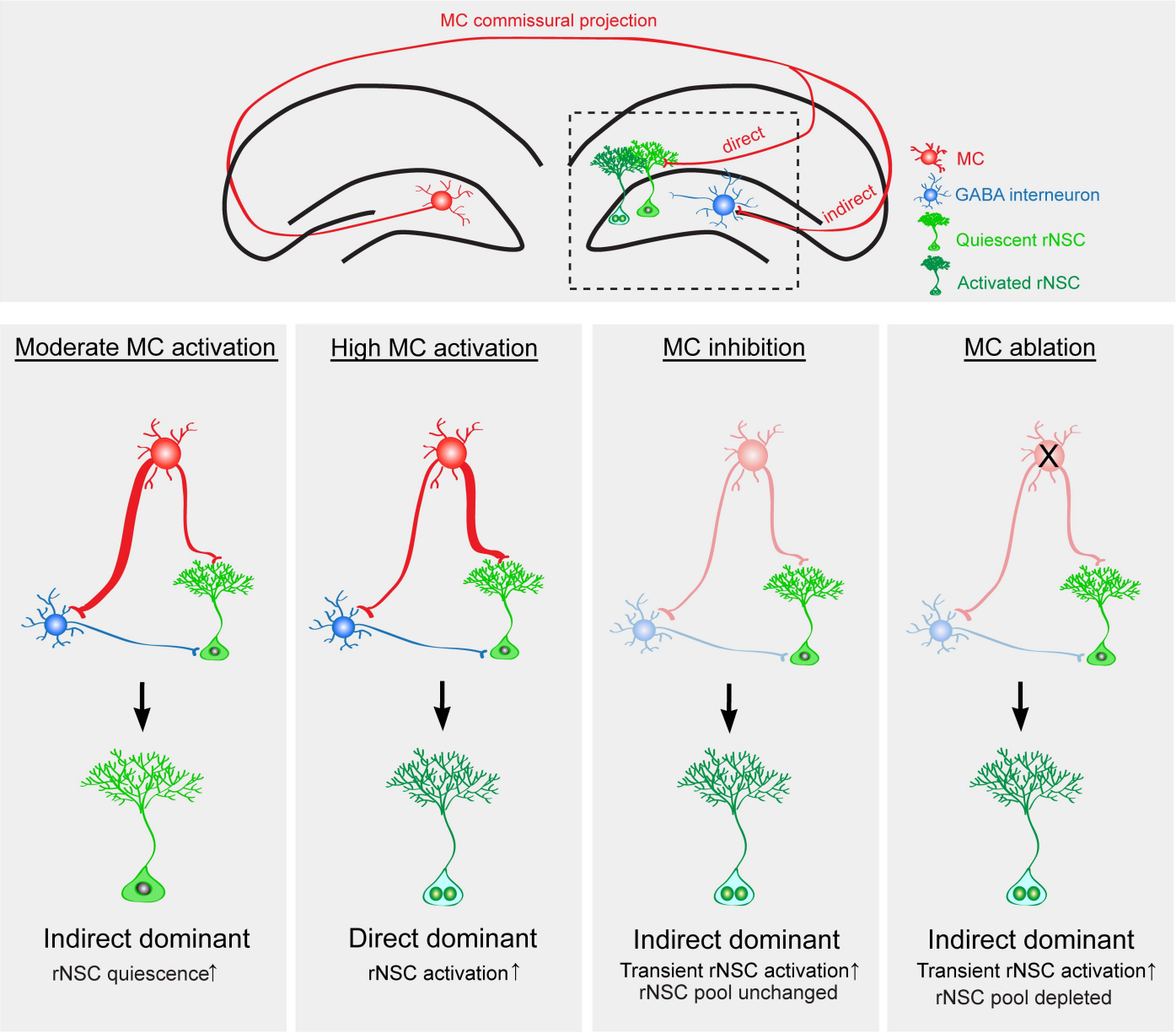


Figure S7. Yeh et al. 2018

**Supplemental Figure Legends**

**Figure S1. Expression of NMDA NR1 subunits in rNSC fine processes in the inner molecular layer. Related to Figure 1.**

(A) Coronal section of the mouse dorsal DG (GCL, granule cell layer; ML, molecular layer), showing an increased density of NR1-immunogold labelling in the first third of the ML.

(B) Dorsal DG labelled with NR1 immunogold and Nestin-GFP immunoperoxidase (DAB, 3,3-diaminobenzidine chromogen). Box, Nestin-GFP-DAB positive rNSC selected for quantification of NR1 immunogold particles in D,E.

(C) Higher magnification of A (SGZ, subgranular zone).

(D) Higher magnification of B.

(E) Low magnification (1,450×) electron microscopy (EM) image of region corresponding to cell in D; used for tracings, area measurements and immunogold quantification, arrows for comparison.

(F) High magnification (5,800×) images covering same region as D and E; used to instruct tracings, measurements and quantifications.

(G) Representative serial EM image (1 of 10 sampled sections, from 124 across the cell) showing the GCL primary process in blue, perisynaptic ML processes in green, mitochondria in pink, NR1-gold in yellow.

(H) Compressed image of the 10 serial sections sampled for analysis (rNSC process in white, NR1-gold in yellow).

(I-K) Two regions of the GCL primary process of a DAB-peroxidase-labelled rNSC, displaying NR1 gold particles; arrows point to membrane-associated particles and arrowheads to others.

(L-N) Perisynaptic ML rNSC processes displaying membrane-associated NR1 gold particles (arrows), directly apposing asymmetrical (putatively excitatory) synapses between axon terminals (a) and dendritic spines (s; m, mitochondria); M and N shown in two serial sections.

(O) Mean ratios of rNSC and control structure (+, positive; -, negative) gold densities (± standard error of the mean) relative to those of ML rNSC perisynaptic processes (control structure ratios compared to rNSC cell ratio) Scale bars: A, 100 µm; B, 20 µm; C- G, 10 µm; H, 5 µm; I-J, 1 µm; K-M, 0.5 µm.

**Figure S2. Validation of dual viral labeling approach, characterization of rNSC morphological heterogeneity, and confirmation of direct pathway in rNSC depolarization using optogenetic approach. Related to Figure 2.**

(A) Representative confocal image showing colocalization of mCherry signal and HA signal from animals injected with AAV-CaMKII-HA-hM3Dq-mCitrine and AAV-CaMKII-mCherry. Scale bar 100 µm.

(B) Sample confocal image of rNSCs from Nestin-GFP animals depicting the diversity in length of rNSC projections. Only a minority of rNSCs are long enough for the bushy heads reach the inner molecular band and interact with the commissural projections (labeled in red). Scale bar 50 µm.

(C) Proportion of Nestin-GFP$^+$ rNSCs with bushy heads reaching MC commissural projections at the inner molecular layer.

(D) Unilateral injection strategy of CaMKII-ChR2-mCherry in Nestin-GFP mice for acute-slice recording at the contralateral side and ChR2 terminal stimulation with 470 nm light.

(E) A sample fluorescence/DIC image and a representative whole-cell recording of a GFP$^+$ NSCs from the contralateral hemisphere with 470 nm LED light stimulation at 10 Hz in the presence of bicuculline.

(F-G) Sample trace showing GFP$^+$ rNSC responding to (F) single blue light flash or (G) a train of flashes in the presence of bicuculline and low concentration 4-AP.

**Figure S3. CNO-dose dependent effects on MCs and contralateral GCL cells, and effects**

**of enriched environment (EE) on c-Fos expression in MCs and rNSC activation. Related to Figure 4.**

(A) Sample $Ca^{2+}$ signals showing dose-dependent increases in $Ca^{2+}$ events induced by chemogenetic activation of GCaMP6f$^{+}$ hM3Dq-mCherry$^{+}$ MCs.

(B) Percentage of MCs that exhibited distinct $Ca^{2+}$ events during each 10-minute epoch of increased CNO concentrations (0, 0.25 and 1 μM CNO).

(C) Quantification of mean calcium event frequency for 0, 0.25 and 1 μM CNO showing trending increase in detectable calcium events. (n=22 MCs, 2 mice).

(D) Distribution of c-Fos$^{+}$ cells in the inner, middle, and outer GCL.

(E) Confocal images showing Nestin and EdU labelling in the DG; white arrow indicates active NSC (EdU$^{+}$ Nestin$^{+}$) while orange arrow heads point to quiescent NSC (EdU$^{-}$ Nestin$^{+}$). Scale bar 100, 50 μm. Higher magnifications on the right.

(F) Confocal images showing c-Fos expression in MCs (GluR2/3$^{+}$ hilar cells) of mice housed in standard housing conditions (left) and EE (right). Arrows indicate c-Fos$^{+}$ cells. Scale bar 10 μm.

(G-H) Increased percentage of GluR2/3$^{+}$ c-Fos$^{+}$ cells in the hilus after EE (G), despite unaltered number of GluR2/3$^{+}$ cells (H) (n= 4 mice from each housing condition).

(I) Confocal images of c-Fos$^{+}$ PV interneurons from mice under EE conditions. Boxed region is shown in higher magnification on the right. Scale bars 100, 20 μm.

(J) Percentage of PV$^{+}$ c-Fos$^{+}$ cells in the DG is unchanged in EE conditions (n=4 mice from each housing condition).

(K) Stereological quantification of Ki67$^{+}$ rNSCs (n=4 mice from each housing condition).

**Figure S4. Chemogenetic activation of MCs by CNO in acute brain slices. Related to Figure 5.**

(A) Unilateral injection of DIO-hM3Dq-mCherry and DIO-GCaMP6s in the DG of 5htr2A-Cre mice.

(B) Fluorescent images in acute brain slices showing mCherry$^{+}$ GCaMP6$^{+}$ cells in the hilus. Scale

bar 20 μm.

(C) Sample fluorescent images of the cell indicated in the boxed region of B, and diverse $Ca^{2+}$ responses in several MCs evoked by CNO.

**Figure S5. Validation of chemogenetic inhibition of MCs by CNO in acute brain slices, and effects on rNSC activation and maintenance by cell-autonomous deletion of ionotropic glutamate receptors in rNSCs. Related to Figure 6.**

(A) Unilateral injection of DIO-hM4Di-mCherry and DIO-GCaMP6s in the DG of 5htr2A-Cre mice.

(B) Sample images of a $GCaMP6^{+}$ $mCherry^{+}$ MC and CNO dependent $Ca^{2+}$ transients.

(C) Sample fluorescence traces for the three cells indicated in B, depicting the quenching of spontaneous $Ca^{2+}$ events by CNO-induced chemogenetic inhibition of MCs.

(D-H) Selective deletion of ionotropic glutamatergic receptors in rNSCs did not significantly alter rNSC behavior. (D) Breeding scheme and (E) TMX induction/EdU injection paradigm of Gria1-$3^{fl/fl}$; $Grin1^{fl/fl}$ (F4 control) and Nestin-$creER^{T2+/-}$; Gria1-$3^{fl/fl}$; $Grin1^{fl/fl}$ (cKO) mice. (F-H) Stereological quantification of EdU incorporation in density (F) and percentage (G), and the density of $GFAP^{+}$ rNSCs (H) in control and cKO mice (n=5).

**Figure S6. Effects of chronic ablation of MCs on non-rNSC populations. Related to Figure 7.**

(A-D) Stereological quantification of proliferation from several non-NSC populations at various time points after Cre-dependent caspase injections in 5htr2A-Cre animals. (A) density of proliferating $EdU^{+}DCX^{+}$ neuroblasts, (B) density of proliferating $EdU^{+}Tbr2^{+}$ intermediate progenitors, (C) density of $EdU^{+}$ cells, and (D) density of $DCX^{+}$ cells. (n=4,3,4,3 mice in control group; n=4,5,4,4 mice in caspase group).

**Figure S7. Summary model of rNSC regulation by various MC activity states. Related to Figures 1-7.** MC commissural projections provide direct glutamatergic and indirect GABAergic inputs to rNSCs. When MCs are activated at a moderate level, the indirect GABA pathway dominates and promotes rNSC quiescence. When MCs are activated at a high level, the direct glutamatergic pathway dominates and promotes rNSC activation. When MCs are inhibited, decreased GABAergic tone is profound, thus resulting in a transient NSC activation (without depleting the rNSC pool). MC ablation similarly results in profound reduction of the indirect pathway, but results in a transient increase of rNSC activation followed by rNSC pool depletion.